ACS APPLIED BIO MATERIALS

www.acsabm.org Article

Hydrophilic 3D Interconnected Network of Bacterial Nanocellulose/Black Titania Photothermal Foams as an Efficient Interfacial Solar Evaporator

Kallayi Nabeela,[‖] Meghana Namdeo Thorat,[‖] Sumina Nambooorimadathil Backer, Animesh M. Ramachandran, Reny Thankam Thomas, Gopika Preethikumar, A. Peer Mohamed, Adersh Asok, Syed Gulam Dastager,* and Saju Pillai*

Cite This: https://doi.org/10.1021/acsabm.1c00143 Read Online

ACCESS | Metrics & More | Article Recommendations | Supporting Information

ABSTRACT: The design and development of scalable, efficient photothermal evaporator systems that reduce microplastic pollution are highly desirable. Herein, a sustainable bacterial nanocellulose (BNC)-based self-floating bilayer photothermal foam (PTF_b) is designed that eases the effective confinement of solar light for efficient freshwater production via interfacial heating. The sandwich nanoarchitectured porous bilayer solar evaporator consists of a top solar-harvesting blackbody layer composed of broad-spectrum active black titania (BT) nanoparticles embedded in the BNC matrix and a thick bottom layer of pristine BNC for agile thermal management, the efficient wicking of bulk water, and staying afloat. A decisive advantage of the BNC network is that it enables the fabrication of a lightweight photothermal foam with reduced thermal conductivity and high wet strength. Additionally, the hydrophilic three-dimensional (3D) interconnected porous network of BNC contributes to the fast evaporation of water under ambient solar conditions with reduced vaporization enthalpy by virtue of intermediated water generated via a BNC−water interaction. The fabricated PTF_b is found to yield a water evaporation efficiency of 84.3% (under 1054 W m^{-2}) with 4 wt % BT loading. Furthermore, scalable PTF_b realized a water production rate of 1.26 L m^{-2} h^{-1} under real-time conditions. The developed eco-friendly BNC-supported BT foams could be used in applications such as solar desalination, contaminated water purification, extraction of water from moisture, etc., and thus could address one of the major present-day global concerns of drinking water scarcity.

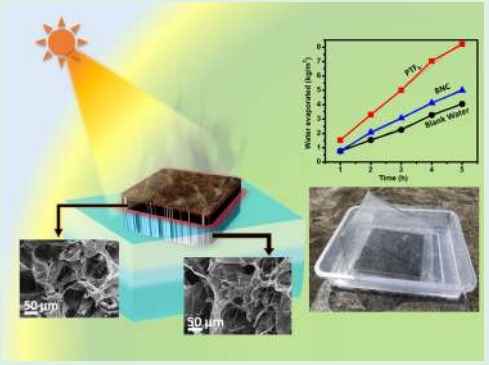

KEYWORDS: *bacterial nanocellulose, black titania, photothermal foam, interfacial heating, solar evaporation*

INTRODUCTION

Recent advances in clean water production technologies demonstrate three-dimensional nanoenabled photothermal systems for efficient solar-light-to-heat conversion.[1−3] Most conventional solar steam generation procedures like solar light concentrators involve heating the bulk water that suffers poor energy efficiency. Interfacial heating and subsequent vapor generation are suggested to resolve this issue.[4,5] Consequently, the last decade has witnessed striking advances in direct solar steam generators. A wide variety of heat-localizing designs were demonstrated to improve the efficiency of clean water production by interfacial heating.[4,6−11] However, the complexity of fabrication methods, the toxicity of materials used, difficulty in scale-up, less durability, etc., dictate the necessity of efficient, scalable, and eco-friendly heat-localizing platforms that provide high water evaporation efficiency.

The solar-energy-harvesting module, the primary component of the solar water generator, should be capable of converting the light into heat energy effectively. From the prior art, nanoenabled photothermal systems, viz. carbon-based materials (e.g., graphene, carbon black, carbon nanotubes, etc.),[4,7,9,12−14] noble-metal nanoparticles (NPs),[6,15,16] MXene (Ti_3C_2),[17] etc., are widely adopted for the research. Among all, nanoenabled metal oxides are considered to be one of the major classes of photothermal materials for fabricating durable and cost-effective clean water evaporators.[5] Generally, metal oxide semiconductor materials absorb solar light to generate electron−hole pairs, which upon recombination through nonradiative relaxation release heat.[18] In this aspect, the discovery of black TiO_2 (BT) has gained considerable attention recently because of its wide-spectrum activity,

Received: February 4, 2021
Accepted: April 13, 2021

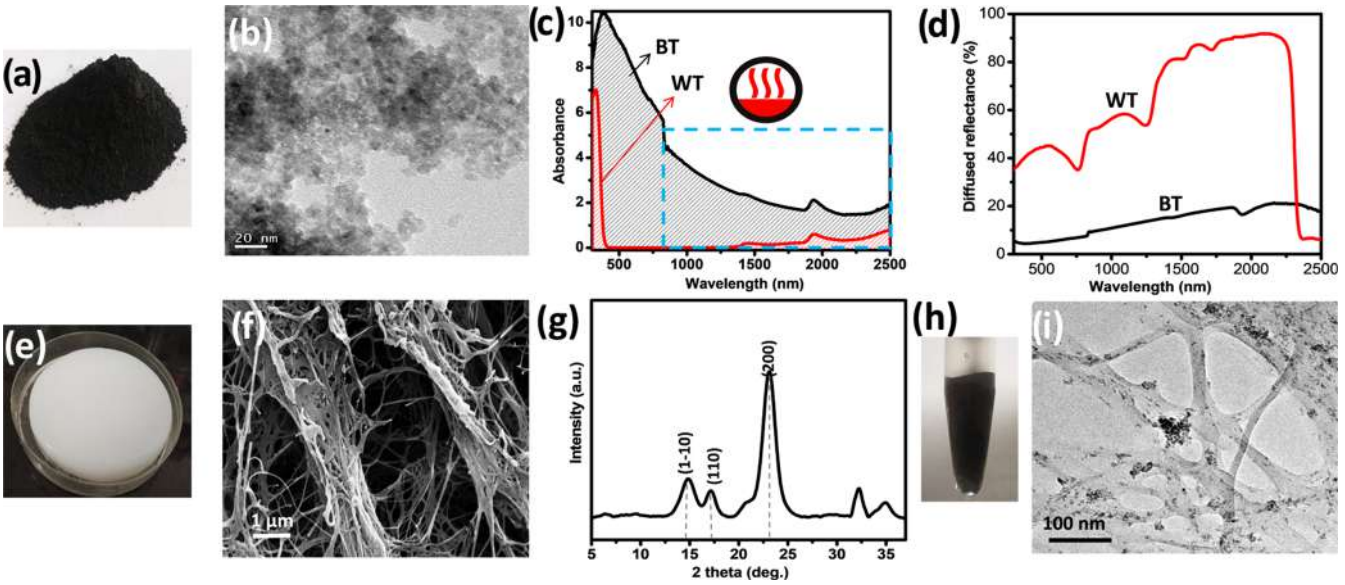

Figure 1. Characterization of BT: (a) digital photograph showing BT powder; (b) TEM image of BTNPs; (c) absorption spectra of BT powder in comparison with those of WT, showing a photothermal region highlighted by a blue dotted box; (d) corresponding diffused reflectance spectra. Characterization of BNC: (e) digital photograph of a BNC pellicle; (f) SEM micrograph revealing the BNC porous nanoarchitecture; (g) XRD pattern featuring characteristic peaks of the cellulose I phase; (h) Digital photograph of a BNC/BT homogeneous aqueous suspension and (i) corresponding TEM image showing the intercalation of BTNPs throughout the BNC matrix.

innocuity, and stability, making it an excellent choice as a photothermal material.[19,20] The enhanced absorption behavior of BT toward the IR region is majorly associated with the introduction of lattice disorders in the crystal lattice via doping, formation of oxygen vacancies, Ti^{3+} formation, etc.[20,21] These form mid-gap energy levels within the band gap of TiO_2, resulting in band-gap narrowing. The BT was for the first time employed for making photothermal sheets by Zhu et al., by which they were able to harvest solar energy for steam generation with an efficiency of 70.9%.[22] Recently, our group has demonstrated a green and straightforward microwave-assisted sonochemical synthesis route for the preparation of BT by the inclusion of Mn^{2+} as a dopant, showing enhanced photothermal conversion ability.[23] The dopant, Mn^{2+}, acts as an oxygen vacancy promoter in the TiO_2 lattice, resulting in the formation of a "state of continuum" in the band gap, thereby extending the absorption to the near-infrared (NIR) region in solar spectra.

Effective thermal management by reducing the radiation and convection loss to the atmosphere as well as the downward conduction loss to the bulk water is the central research goal in the fabrication of an efficacious solar vapor generator for the maximum utilization of solar energy.[8,24] Consequently, diverse designs were proposed, including three-dimensional morphologies capable of recycling the incident radiation within the porous blackbody channels,[9,25,26] use of thermal insulating materials to prevent the downward conduction loss,[13] etc. Generally, most of the nanoenabled photothermal materials often require a lightweight support like polymers to make them porous, flexible, floatable, and/or easily moldable.[5,14] Furthermore, bringing down the energy demand for water evaporation by virtue of a water−polymer interaction in polymeric hydrogels containing hydrophilic functional groups is another modernistic and revolutionary approach to achieve augmented evaporation rate.[27−29] Thus, hydrophilic polymers like poly(vinyl alcohol) (PVA), chitosan, etc., were already proven to have the potential to outperform most conventional hydrophobic polymers like poly(vinylidene fluoride) (PVDF),[10,19,30,31] polystyrene (PS),[32] polypyrrole (PPy),[11] polyurethane (PU),[33] etc. Zhao and co-workers reasoned the reduction in water evaporation enthalpy by water activation through the formation of intermediate water by a water−polymer (PVA) interaction.[27,29]

Evaporators based on sustainable materials like cellulose-based papers,[34,35] wood,[36,37] foams,[38−40] etc., have been utilized as a promising green substitute over synthetic polymers in the last few years for contemporary designs of solar-driven pure water generators by various groups.[41,42] Among them, nanocellulose fibers hold the "nano" advantages of a matrix with a large number of surface −OH functionalities for developing high-performing nanoenabled photothermal systems. In this respect, mechanically strong, flexible, and thermally stable bacterial nanocellulose (BNC) could be a green alternative for the existing polymers or dispersants capable of hosting BT nanoparticles (BTNPs), maintaining its porous nanonetwork structure with excellent wet strength and biocompatibility.[43,44] A number of studies have proven BNC as a promising porous scaffold capable of accommodating a variety of photothermal entities yielding superior solar evaporators with a noteworthy improvement in their overall solar evaporation performance.[13,38,39,45−48] Regardless of the culture media, this material possesses high purity and biocompatibility among the materials of its kind, which is an additional advantage in applications like clean water production. Accordingly, the use of the BNC matrix for the inclusion of BTNPs can yield a promising scalable and sustainable photothermal system.

Herein, we report a superior self-floating nanoarchitectured bilayer photothermal foam (PTF_b) composed of wide light-absorbing BTNPs and a BNC hydrogel for clean water production. BTNPs incorporated into the BNC matrix constitute a highly porous top solar-harvesting layer that enables efficient interfacial vapor generation with reduced energy consumption, whereas a pristine BNC bottom layer

https://doi.org/10.1021/acsabm.1c00143
ACS Appl. Bio Mater. XXXX, XXX, XXX−XXX

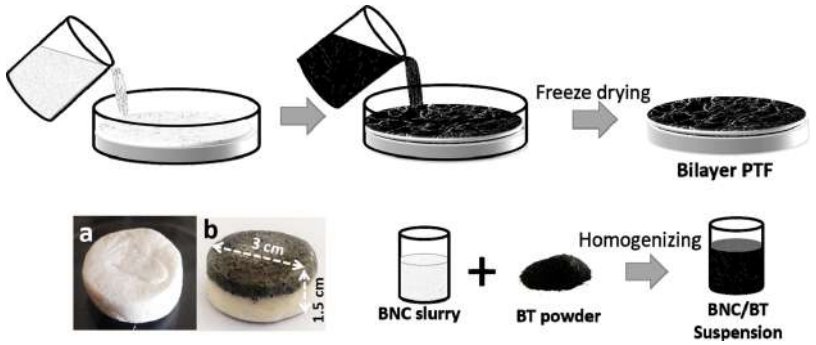

Figure 2. Scheme showing the fabrication of bilayered PTFs. Digital photographs of (a) control BNC foam and (b) bilayer PTF.

facilitates upward water transport while serving as a hydrophilic thermal insulating floating support.

RESULTS AND DISCUSSION

Characterization of BT and BNC. BT, prepared by the microwave-assisted sonochemical method discussed in our previous report, is a black powdery (a digital photograph is given in Figure 1a) semiconductor material showing broad-spectrum absorption.[23] The size of BTNPs is 5−8 nm, as revealed from the transmission electron microscopy (TEM) analysis (Figure 1b). Upon drying, they tend to form agglomerates, as seen in scanning electron microscopy (SEM) micrographs (Figure S1a, Supporting Information). The tetragonal structured anatase phase of BT was validated with the powder X-ray diffraction (XRD) pattern presented in Figure S1b, Supporting Information. The diffraction peaks observed at 25.3, 37.8, 48.1, and 54.4° are assigned to (101), (004), (200), and (105) diffracting planes, respectively (JCPDS #21-1272; standard spectral data is marked as a blue line plot for comparison). Figure 1c shows the NIR absorption spectra recorded for BT powder and their comparison with those of white titania (WT) powder,[49] showing extended absorption of BT in the NIR range (see the red marked region in absorption spectra, Figure 1c). The corresponding diffused reflectance spectra (Figure 1d) show a negligible reflection loss for BT, making it an attractive photothermal material for the anticipated application. However, its materialization confronts problems because of its poor dispersibility in aqueous media as well as in most common solvents. Nevertheless, BNC was found to act as a green aqueous dispersant for BTNPs.

BNC was obtained in the form of a thick pellicle at the liquid/air interface by the culturing of the *Komagataeibacter rhaeticus* PG2 strain.[50] The digital photograph of a BNC pellicle obtained is given in Figure 1e. The robust network structure of a representative lyophilized BNC pellicle could be seen in the SEM micrograph given in Figure 1f. The TEM image of BNC fibers (provided in Figure S2a, Supporting Information) obtained from a very dilute aqueous suspension of BNC (Figure S2a, inset, Supporting Information) shows that the length of fibrils ranges from 0.5 to 3.5 μm and the width from 30 to 70 nm. The length and width distributions of BNC are represented as histograms, as shown in Figure S2b,c (Supporting Information), respectively. A high crystallinity of 74.6% was obtained for BNC, as calculated from wide-angle X-ray scattering (WAXS) analysis (Figure 1g), adopting a deconvolution method for amorphous and crystalline peaks.[51] The as-obtained diffraction pattern features characteristic peaks of the native cellulose I allomorph, positioned at 14.8, 17.1, and 23.1°, originating from $(1\bar{1}0)$, (110), and (200) planes, respectively.[50,52] Furthermore, on a closer examination of the attenuated total reflectance-Fourier transform infrared (ATR-FTIR) spectrum of lyophilized BNC (Figure S2d, Supporting Information), we could observe two weak, yet noticeable, vibrational peaks at 750 and 710 cm^{-1}, characteristic of cellulose Iα and Iβ phases, respectively.[53] For clarity, the marked red dotted box from 950 to 650 cm^{-1} in the ATR-FTIR spectrum is enlarged and presented in Figure S2e, Supporting Information.

Subsequently, the incorporation of photothermally active BTNPs into the BNC matrix was carried out by homogenization, resulting in a stable gel-like dispersion. Figure 1h is the digital photograph showing a homogeneous aqueous slurry of BTNPs in the BNC matrix. The TEM image given in Figure 1i shows that BT is embedded throughout the BNC matrix. It is presumed that BT with a positive surface charge [zeta (ζ)-potential value of BTNP: +12.0 ± 0.3 mV] is more likely to adhere to the electron-rich cellulose fibril surface (ζ-potential value of BNC: −12.9 ± 2.6 mV), ensuring less leaching of photoactive material from the fabricated PTF.

Fabrication and Characterization of BNC/BT-Based PTFs. As discussed before, interfacial heating is the most energy-efficient route for designing an outright solar evaporating system, and a porous three-dimensional floating model can therefore yield a better performing solar vapor generator.[1,42,54] Accordingly, the use of the three-dimensional (3D) interconnected porous network of BNC as a matrix for hosting wide-spectrum active BTNPs can engender an improved energy-efficient photothermal system. The homogenous BNC/BT mixtures in desired ratios were lyophilized to obtain highly porous, lightweight PTFs. However, we observed that, unlike a pristine BNC foam, a BNC/BT foam was unable to float. The drowning nature of single-layered PTF is attributed to the dense loading of BTNPs onto the BNC network structure. Nevertheless, we found that providing a thicker BNC bottom layer could keep PTF afloat at the air/water interface. The digital photographs of floatability experiments are demonstrated in Figure S3, Supporting Information. By providing an additional thermal insulating layer, the conduction heat loss toward the bulk water can be minimized.[13] Here, the thermal conductivity of the bottom BNC layer was measured as 0.066 W m^{-1} K^{-1}. A scheme illustrating the fabrication of bilayer BNC/BT PTF is given in Figure 2. The bilayer foams were fabricated by casting a BNC/BT slurry on a wet BNC-alone layer followed by lyophilization. For comparison, a pristine BNC foam of the same dimensions was also prepared as a control sample. The digital photographs

https://doi.org/10.1021/acsabm.1c00143
ACS Appl. Bio Mater. XXXX, XXX, XXX−XXX

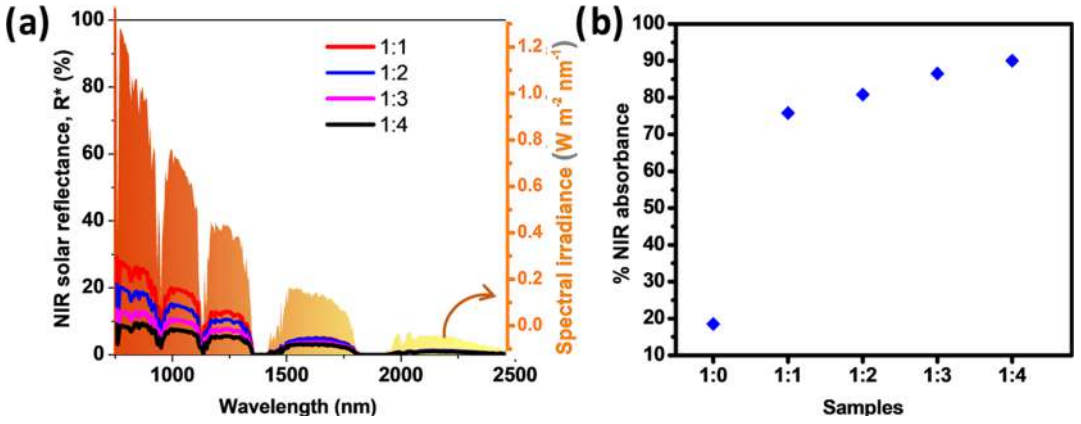

Figure 3. (a) NIR solar reflectance spectra of PTFs prepared with varying BNC/BT compositions; the shaded area is the solar spectral irradiance. (b) Percentage NIR absorption plot for PTFs with varying BNC/BT compositions.

of fabricated BNC foam and bilayer BNC/BT PTFs are presented in Figure 2a,b, respectively. The bilayer BNC/BT PTFs fabricated with varying BNC/BT compositions (1:0, 1:1, 1:2, 1:3, and 1:4 wt %) are shown in Figure S4a, Supporting Information. We observed that BTNP loading higher than 4 wt % resulted in dense and deformed PTFs. A regular gradation in black color as the BT loading increases on the top solar-harvesting layer was noted. Figure S4b–f shows the SEM micrographs of top layers of fabricated bilayer PTFs with BNC/BT wt % ratios of 1:0 (control pristine BNC foam), 1:1, 1:2, 1:3, and 1:4, respectively, revealing changes in their porous architectures upon BT incorporation. The observed reduction in porosity could be attributed to the dense packing of BTNPs into the BNC network.

Further, NIR absorption spectra were examined and the percentage NIR absorptions were calculated for the as-fabricated PTFs. The NIR solar reflectance spectra are presented in Figure 3a. Figure 3b is the percentage NIR absorption plot for different PTFs with varying compositions. The percentage absorption values for varying BNC/BT compositions are tabulated in Table 1. Apparently, 4 wt % BT loading on the top layer (i.e., BNC/BT ratio 1:4) was found to show a higher percentage of solar absorbance (90.0%) and minimized solar reflectance compared to other compositions. The light-to-heat conversion performance of as-prepared PTFs was also tested by exposing the top surface to ∼1000 W m^{-2} solar illumination for 1 h. Thermal profiles of PTFs of different compositions in the dry state before and after illumination are presented in Figure S5a,b. A control BNC foam is also kept for reference. In agreement with the above findings, the highest temperature rise was observed for the sample with the highest BT loading and hence the optimum 1:4 BNC/BT composition was selected for further studies. For convenience, bilayered PTF with an optimized composition is termed hereafter as PTF_b.

Table 1. Percentage Absorption Values Calculated for PTFs Prepared with Varying BNC/BT Compositions

BNC/BT	% absorption
1:4	90.0
1:3	86.6
1:2	80.8
1:1	75.8
1:0	18.5

Characterization of the PTF_b Foam. Further, we characterized each layer in more detail to elucidate the porous structures of PTF_b, and the results are consolidated in Figure 4. A digital photograph of PTF_b is provided in Figure 4a. A closer examination of both layers of PTF_b using SEM is presented in Figure 4b–e. The results revealed a dense distribution of BTNPs onto the BNC fibrous network in the top solar-harvesting layer (Figure 4b) that considerably reduces the pore size, as seen in Figure 4c. Figure 4d,e shows the SEM micrographs of the pristine BNC bottom layer under different magnifications, showing highly interconnected 3D porous cellular structures that are both macro- and mesoporous in nature.

Furthermore, for a profound understanding of porosity and surface area, nitrogen adsorption and desorption experiments were conducted. The average Brunauer–Emmett–Teller (BET) surface area and Barrett–Joyner–Halenda (BJH) pore size distributions obtained for both layers of PTF_b are consolidated in Figure S6, Supporting Information. The BET adsorption isotherms of top and bottom layers are presented in Figure S6a, Supporting Information, and Figure S6b, Supporting Information, respectively. A remarkably high surface area of 127.3 m^2 g^{-1} is observed for the top solar-harvesting layer, suggesting that additional sites were being made available for interfacial heating by virtue of BT nanoparticles decorated onto the BNC network. The comparatively low surface area of the bottom layer (≈16.0 m^2 g^{-1}) may have resulted from the open porous structure of the pristine BNC foam. It is apparent from the nitrogen adsorption–desorption results that both layers show considerable deviations from type IV isotherms (type IV isotherms are characteristic of mesoporous materials). The likely explanation for this deviance could be made by the coexistence of pore sizes ranging from meso to macro, as calculated from corresponding BJH pore volume plots of both layers (Figure S6c,d). However, it is noteworthy that the deviation is pronounced for the bottom layer (BNC) due to a large pore volume fraction in the macro range (average pore diameter, 16.4 nm) compared to that for the top layer. On the other hand, the BJH pore volume plot of the top layer (Figure S6d) proves the existence of a large fraction of pores with sizes ranging from 2 to 10 nm (average pore diameter: 4.6 nm). Wettability studies using a sessile drop water contact angle

https://doi.org/10.1021/acsabm.1c00143
ACS Appl. Bio Mater. XXXX, XXX, XXX–XXX

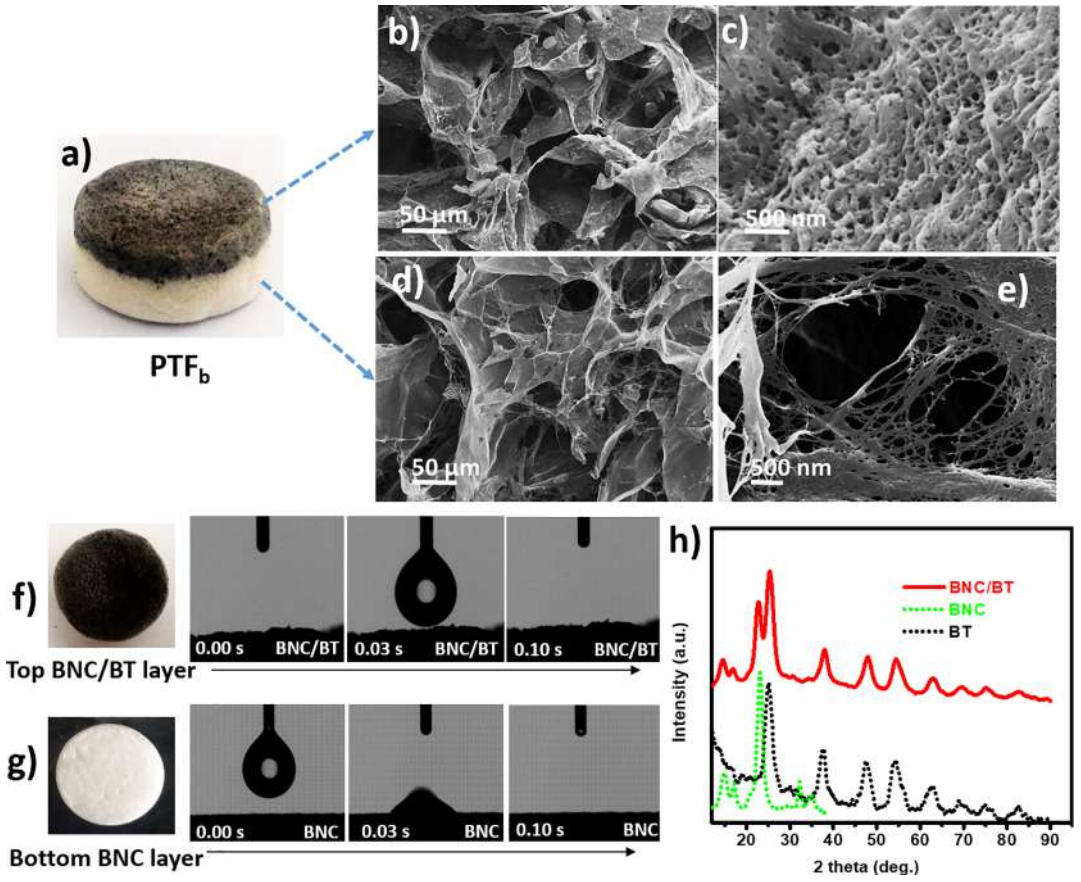

Figure 4. (a) Digital photographs of PTF_b. SEM micrographs of PTF_b taken for (b) and (c) BT-rich top layer and (d) and (e) pristine BNC bottom layer under different magnifications. Highly porous nature of PTF_b revealed by wettability studies performed using a contact angle instrument on (f) solar-harvesting top layer and (g) pristine BNC bottom layer. (h) XRD pattern of the BNC/BT top layer (red plot) featuring diffracting planes of BNC and BT. The green dotted pattern and the black dotted pattern correspond to control BNC and BT samples, respectively.

experiment on both layers were further conducted to demonstrate the superhydrophilic nature of fabricated PTF_b. The superhydrophilic nature of the BNC/BT foam (Figure 4f) and BNC-alone layer (Figure 4g) is evident from the instantaneous imbibition of a water drop. Apparently, the highly porous nature (as revealed from the SEM observations) of the fabricated PTFs also contributes to the rapid infusion of water. This will enhance faster transportation of water to the points of interfacial heating and therefore elevate the evaporation rate. Figure 4h presents the XRD pattern of the BNC/BT composite layer, featuring characteristic diffraction peaks of BNC and BT. For comparison, XRD patterns of control BNC (green dotted plot) and BTNPs (black dotted plot) are also provided.

Photothermal Studies Using BNC/BT-Based PTFs. The photothermal conversion of the fabricated PTFs was monitored by thermal profiling using a thermal imaging camera before and after 1 h light exposure under a simulated solar irradiance of 1054 W m^{-2} power density. The evaporation performance of bilayered PTFs with optimized compositions was compared with that of two control experiments: a pristine BNC foam and the same volume of blank water (without PTF). Thermal profiling was done to monitor the temperature rise in PTFs at the air−water interface and the bulk. Figure 5a is the aerial-view thermal image of PTF_b. The side-view thermal profile of the beaker presented in Figure 5b substantiates the effective localization of heat generated at the PTF−water interface (marked in a green dotted circle). Digital photographs of the same are also provided for better understanding. Further, the evaporation performance of the fabricated PTFs was tested under simulated conditions. Figure 5c is the cumulative mass of water evaporated vs time plot for PTF_b, the control pristine BNC foam, and blank water (without PTF). The rates of evaporation were calculated from the corresponding linear fit. It was found that the water evaporation rate of PTF_b (≈1.71 kg m^{-2} h^{-1} at 1054 W m^{-2} sun power density) was at least twice that of blank water under identical conditions. In Figure 5c, it is noteworthy that there is an increase in the evaporation rate with the pristine BNC hydrogel (even in the absence of any photothermal materials) compared to that with blank water.

A differential scanning calorimetry (DSC) experiment was carried out to obtain the evaporation enthalpy of the BNC/BT hydrogel system, and the thermograms are given in Figure 5d. It is insightful to demonstrate the impact of a BNC−water interaction on the total evaporation performance in BNC/BT PTFs. Unlike the sharp peak observed for pure water, the evaporation peak of the BNC/BT hydrogel showed considerable broadness. This may be due to the fact that the liquid-to-gas transition happened sharply at the boiling temperature in the case of free-state water and declined right away. However, the evaporation started with less required energy in the latter system and declined gradually after reaching a maximum. It is remarkable that the completion of evaporation still happens at a higher temperature attributed to the high

https://doi.org/10.1021/acsabm.1c00143
ACS Appl. Bio Mater. XXXX, XXX, XXX−XXX

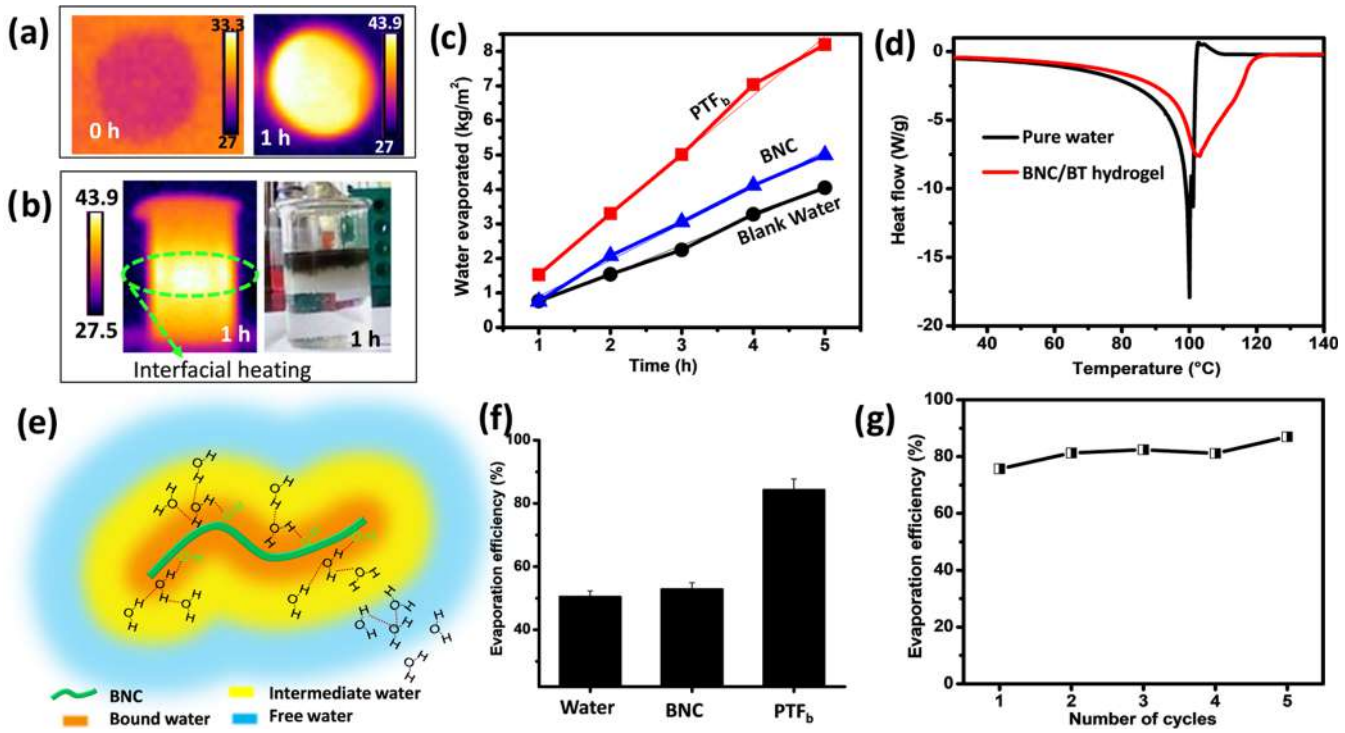

Figure 5. IR thermal images of wet PTF_b taken before and after 1 h illumination: (a) top-view and (b) side-view thermal profiles of a beaker after illumination showing interfacial heating marked with a green dotted circle; a digital photograph of the side view is shown on the right side. (c) Cumulative mass of water evaporated vs time plot. (d) Differential scanning calorimetry (DSC) heat flow vs temperature DSC curves showing a difference in the nature of evaporation in a BNC/BT hydrogel and pure water. (e) Schematic representation of the occurrence of three states of water in a BNC hydrogel. (f) Bar diagram showing the variation in solar water evaporation efficiencies of PTF_b, the control pristine BNC foam, and blank water (without PTF). (g) Cyclic performance of PTF_b carried out for five cycles. Solar illumination power density: ~1 kW m^{-2}.

energy required for the evaporation of bound water. Nevertheless, the calculation shows that the overall h_{LV} of water from the BNC/BT hydrogel was obtained from DSC as ≈1870 kJ kg^{-1}, quite lower than that of free water evaporation enthalpy (≈2307 kJ kg^{-1}, close to the theoretical value). The difference in evaporation peaks corresponding to the BNC/BT hydrogel and pure water suggests the difference in the nature of water evaporation from both systems. From the prior art, the broadness of the evaporation curve signifies the existence of different possible water states, owing to the cellulose polymer−water interaction.[27,28]

Figure 5e portraits a symbolic representation of different water states in the BNC hydrogel system. Having a large number of −OH surface functionalities, the BNC network is highly susceptible to hydration, forming the least evaporable bound water (see the orange zone in Figure 5e). Therefore, one can anticipate a second state of intermediate water called the activated water form (see the yellow zone in Figure 5e) with reduced h_{LV} as a result of its weak bonding to the adjacent bound water molecules. These water molecules hence require quite low energy for the liquid−vapor transition than the standard evaporation enthalpy of free water. A considerable reduction in the h_{LV} of water was hence observed with the BNC/BT hydrogel system.

A bar diagram showing the efficiencies of the three systems is given in Figure 5f. PTF_b shows a solar conversion efficiency of 84.3%. Further, to test the durability and sustainability of the fabricated photothermal system, a cyclic study of PTF_b was conducted. The corresponding plot is presented in Figure 5g, revealing a consistent performance of the bilayer system up to five cycles. The results strongly suggest PTF_b as a promising solar water evaporator for freshwater production that will curb microplastic pollution to a certain extent. Both evaporation rate and evaporation efficiencies calculated for PTF_b, the control pristine BNC foam, and blank water from the mass loss of water are tabulated in Table 2.

Table 2. Evaporation Rates Calculated from the Slopes of Corresponding Linear Fits of the Mass of Evaporated Water vs Time Plot with Their Calculated Solar Evaporation Efficiency Values[a]

material	evaporation rate (kg m^{-2} h^{-1})	evaporation efficiency, η (%)
BNC/BT PTF_b	1.71 ± 0.07	84.3 ± 3.4
pristine BNC	1.05 ± 0.04	52.9 ± 2.0
blank water	0.83 ± 0.03	50.5 ± 1.8

[a] h_{LV} values were obtained from corresponding DSC data.

The above findings reveal the factors that lead to the augmented evaporation performance of PTF_b and advocate BNC as a promising sustainable matrix for the fabrication of lightweight bilayer PTF. It could be seen that mere overloading of BTNPs on the top solar-harvesting layer did not result in an improved evaporation rate (maximum 8 wt %, a photograph of the bilayer foam with the 1:8 BNC/BT composition is given in Figure S7, Supporting Information). Thus, multiple advantages envisioned for BNC being used as a platform for the inclusion of BT nanoparticles toward solar vapor generation are as follows: (1) The highly entangled BNC/BT network rendered a mesoporous as well as a macroporous 3D nanoarchitecture, which trapped incident solar light, creating extensive internal

https://doi.org/10.1021/acsabm.1c00143
ACS Appl. Bio Mater. XXXX, XXX, XXX−XXX

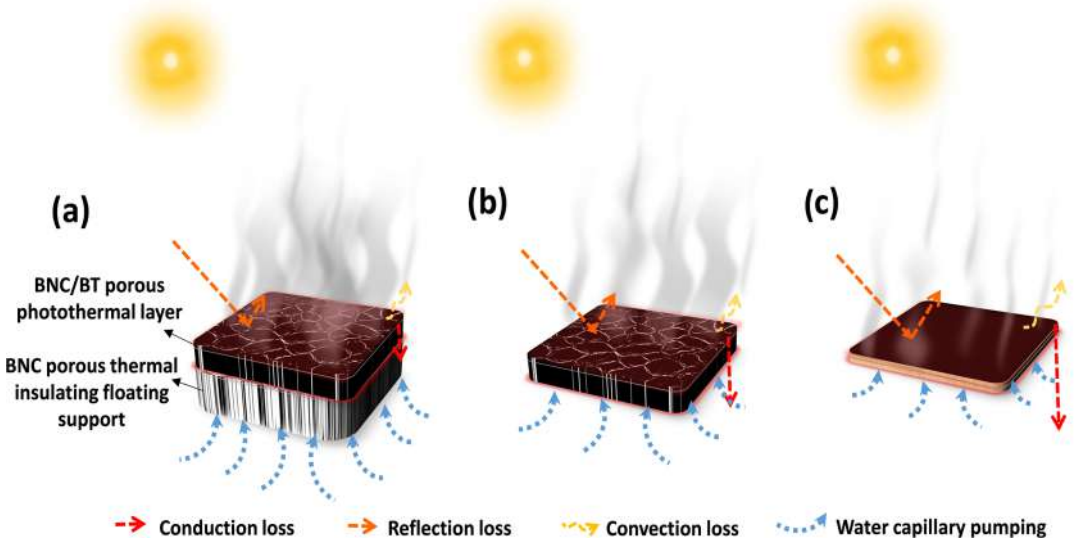

Figure 6. Symbolic schematic representation of effective thermal loss management in (a) bilayer BNC/BT PTF, (b) single-layered BNC/BT PTF, and (c) 2D BNC/BT sheet.

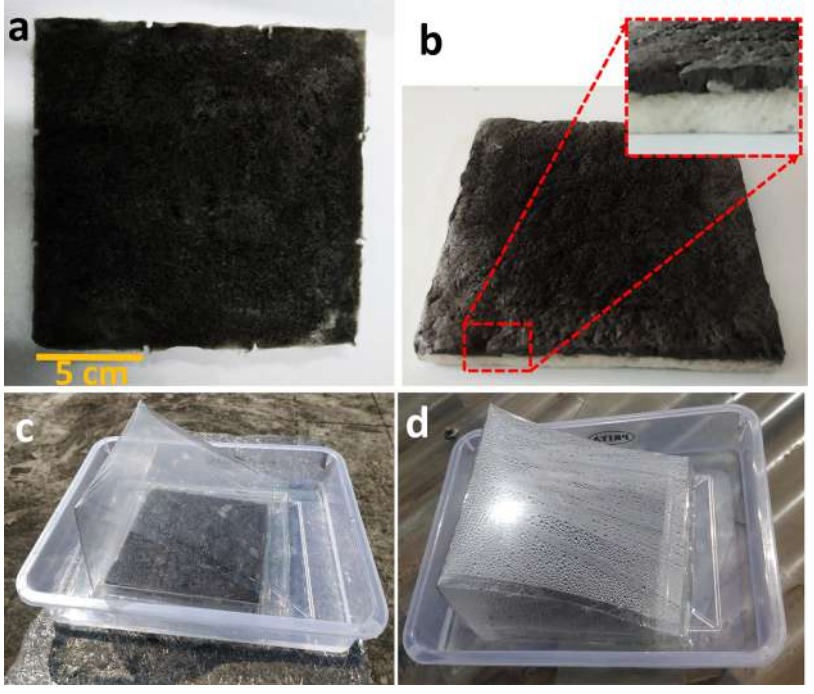

Figure 7. Digital photographs showing (a) top view and (b) side view of PTF_b fabricated in larger dimensions (15 × 15 cm^2). The evaporation chamber with PTF_b used for water collection under real-time conditions (c) before and (d) during water vapor generation. Solar power density: 1 sun.

reflections inside the pores, leading to effective light absorption (or a diminished reflection loss). Unlike flat surfaces, the porous BNC foam has minimal dependence on the incident radiation angle. This is important in real-time applications since the solar light incident angle keeps on varying with time and season.[54] (2) The thermal insulating BNC network that has been used herein can act as a thermal barrier for the heat generated, resulting in a reduced conduction loss toward bulk water. The top solar-harvesting BNC/BT layer itself has a thermal conductivity as low as 0.040 W m^{-1} K^{-1}. (3) The BNC skeleton could act as a hydrating frame, which helps in the formation of activated water by generating a significant amount of intermediate water, and thus minimize the energy requirement for the evaporation of water considerably. (4) An added benefit is highlighted by the use of a superhydrophilic BNC foam that possesses numerous continuous porous channels, which help the smooth diffusion of water from the bulk to evaporating interfaces. This fast capillary pumping effect has a significant influence on improving the efficiency of the solar distillation process. Figure 6 schematically illustrates the advantages of a bilayer PTF over single-layered PTF and a two-dimensional (2D) BNC/BT sheet in terms of improved thermal management and capillary rise.

Real-Time Experiment. Further, we successfully scaled-up the BNC/BT PTF_b to 15 × 15 cm^2 dimensions (digital photographs of PTF_b sheet are depicted in Figure 7a,b) and

https://doi.org/10.1021/acsabm.1c00143
ACS Appl. Bio Mater. XXXX, XXX, XXX−XXX

demonstrated its applicability for pure water production. An experimental setup of the photothermal water production prototype is shown in Figure 7c. The feed water was initially filled in the tray, and PTF_b stayed afloat. The condensation-water collection chamber was then covered over it. The setup was then placed outdoor for 6 h on a sunny and clear day. The water vapors produced were condensed on the surface of the slanting roof and collected at the side chamber (Figure 7d). The water collection values were normalized to a sun power density of 1000 W m^{-2} for comparison purposes. The real-time experiment yielded a total freshwater collection of 1.26 L m^{-2} h^{-1}.

CONCLUSIONS

In summary, we fabricated environmentally benign, scalable, and tunable nanoarchitectured bacterial nanocellulose/black titania bilayer PTF as a superior photothermal material and used it for freshwater production by efficient interfacial heating. PTF_b was designed in such a way that the top solar-harvesting layer constituted wide-spectrum active BTNPs incorporated into the BNC matrix below which a thick layer of pristine BNC was provided. The porous BNC/BT top layer helped in efficient photothermal energy conversion and induced interfacial water heating at the PTF/water interface, whereas the pristine BNC bottom layer played a dual role as an efficient thermal barrier for reduced energy loss and as a porous floating support. The highly hydrophilic interconnected porous BNC channels facilitated the capillary rise of bulk water, aiding the effective evaporation of water via the interfacial heating process. Besides, the BNC skeleton acted as a hydrating network that could induce the formation of activated water by generating a significant amount of intermediate water by virtue of a BNC−water interaction and thus minimize the energy requirement for the evaporation of water (i.e., h_{LV}) considerably. Among a series of foams with varied BNC/BT ratios, 4 wt % BT loading on the top layer demonstrated a better photothermal efficiency of 84.3%. Finally, the optimized PTF_b was successfully fabricated for a large area, 15 × 15 cm^2, for solar freshwater production with a water collection rate of 1.26 L m^{-2} h^{-1} (under 1000 W m^{-2}). Thus, the BNC/BT bilayer PTF design could be a promising, scalable, and sustainable solution for clean water production with excellent photothermal conversion efficiency with minimal heat loss and better scalability.

EXPERIMENTAL SECTION

Materials. Purified wet BNC pellicles were prepared as described in our previous report.[50] Black TiO_2 (BT) was prepared by microwave-assisted sonochemical synthesis using titanium isopropoxide ($Ti[OCH(CH_3)_2]_4$) as a precursor and Mn^{2+} as a dopant.[23] The BT flakes were ground to a fine powder and used without further modifications. White titania (WT) was prepared by the method adopted by Sumina et al.[49]

Preparation of Bacterial Nanocellulose (BNC). BNC was produced using the *K. rhaeticus* PG2 strain isolated from a rotten pomegranate in a modified Hestrin−Schramm (HS) medium containing glycerol as a carbon source. The detailed procedure is given elsewhere.[50] The purified BNC pellicle was stored under 4 °C for further use.

Fabrication of BNC/BT Photothermal Foams. Wet BNC pellicles were ground in a homogenizer (DLAB OS40pro) at 800−900 rpm to make a 2% (corresponds to dry weight) BNC slurry. For preparing homogenous BNC/BT mixtures in desired proportions, dry fine powdered BT was mixed with the above-prepared BNC suspensions at BNC/BT ratios of 1:1, 1:2, 1:3, and 1:4 using a lab blender. For bilayered PTFs, a thick layer of a pure BNC slurry was first transferred in a 3 cm diameter mold, followed by a BNC/BT mixture. The bottom layer and top layer thicknesses were maintained as ∼1 and 0.5 cm, respectively, for all PTFs. A control BNC foam without the incorporation of BT, maintaining similar dimensions, was also molded for comparison. The cast hydrogels were then lyophilized to get aerogels.

Characterizations. The morphological analysis of the BT powder, BNC foam, and PTFs was carried out using an EVO 18 special edition scanning electron microscope, Carl Zeiss, Germany, with an accelerating voltage of 10 kV. SEM samples were prepared by cutting dry PTFs using a sharp razor and stuck on a carbon tape. Samples were gold-sputtered prior to the imaging to avoid charging. Long BNC fibers and the distribution of BT in the BNC matrix were visualized on an FEI Tecnai 30 G2S-TWIN transmission electron microscope operated at an accelerating voltage of 300 kV. TEM sample preparations were done on a carbon-coated copper grid by drop-casting two to three drops of the sample solution. A dilute homogeneous aqueous suspension was prepared by derivatizing the BNC by TEMPO oxidation[55,56] and analyzed using TEM under stained (using 1% phosphotungstic acid) conditions. Drying was done at room temperature. The crystallinity of BNC was determined from the wide-angle X-ray scattering (WAXS) measurements carried out on a Xeuss SAXS/WAXS system using a Genisxmicro source from Xenocs operated at 50 kV and 0.6 mA. The powder X-ray diffraction (XRD) pattern of the BT sample was taken on a PANalytical Empyrean instrument equipped with reference radiation of Cu Kα (λ = 1.54 Å) at an operating voltage of 45 kV. The attenuated total reflectance-Fourier transform infrared (ATR-FTIR) spectra were recorded with a PerkinElmer series Spectrum Two FTIR spectrometer over the wavenumber range of 4000−500 cm^{-1}. ζ-Potential measurements were done using a Nano ZS Malvern instrument. The thermal conductivity of BNC and BNC/BT foams was checked on Unitherm 2022, Anter Corp, using the hot plate method (ASTM E-1530). Two plates, namely, a hot plate and a cooling plate, are built in this instrument. A sample aerogel disc (50 mm diameter, 13 mm thickness) was placed between the two plates, where one plate had been heated and the other plate had been cooled. The temperature of the plates was noted till they attained a steady state. The thermal conductivity of the samples was then calculated from the steady-state temperatures, dimension of the sample, and heat input. Absorption, total reflectance, and diffuse reflectance spectra (DRS) of PTFs were recorded in the 200−2500 nm range, using a UV−VIS−NIR spectrometer (UV-2600). The measurements were corrected by the baseline/blank correction. The NIR solar reflectance (R^*) was measured using the solar spectral irradiance in the range 700−2000 nm. The solar absorptions "A" of samples in the 700−2000 nm region were measured using eq 1.

$$A = \frac{\int (1 - T)\cdot S \cdot d\lambda}{\int S \cdot d\lambda} \quad (1)$$

where T is the reflectance of the sample, S is the solar spectral irradiance (W m^{-2} nm^{-1}), and λ is the wavelength. The wettability of samples was checked using a contact angle goniometer (KYOWA, DMe-201) by sessile-dropping water (2.0 μL) droplets on the porous BNC/BT foams. The specific surface areas of the bilayer aerogels were measured by the Brunauer−Emmett−Teller (BET) method using Autosorb-1C (AX1C-MP-LP) at 298 K. The pore size distribution was obtained by the Barrett−Joyner−Halenda (BJH) method.

Estimation of Photothermal Energy Conversion. The photothermal energy conversion from solar light into heat for vapor generation was calculated from the amount of evaporated water. The mass difference with and without BNC/BT PTFs under ∼1000 W m^{-2} was assessed, and the rate per unit area was calculated for each sample. The power required for the evaporation of water (Q_e) was measured using eq 2.[31]

https://doi.org/10.1021/acsabm.1c00143
ACS Appl. Bio Mater. XXXX, XXX, XXX−XXX

$$Q_e = \frac{m \times h_{LV}}{t}(\%) \quad (2)$$

where m is the mass of evaporated water per unit area, t is the time, and h_{LV} is the enthalpy of vaporization of water from a hydrogel system, obtained directly from a differential scanning calorimetry (DSC) thermogram of the corresponding hydrogel sample,[27,28] acquired on a PerkinElmer DSC 8000 instrument at a heating rate of 10 °C min^{-1} under a nitrogen flow. The h_{LV} of free water was also calculated for comparison from the thermogram of pure water.

If Q_s is the power of incident solar radiation monitored in a solar power meter (Newport Instruments, 91159A), the solar evaporation efficiency (η) is obtained as the ratio of Q_e and Q_s (eq 3).[31]

$$\eta = Q_e/Q_s \quad (3)$$

The final equation for η in percentage takes the form given in eq 4.[26,57]

$$\eta = \frac{m \times h_{LV}}{I \times t}(\%) \quad (4)$$

where $Q_s = I$ is the incident solar power density.

Solar Evaporation Experiments. The evaporation experiments were performed at room temperature under a xenon lamp (250 W) solar simulator coupled with a Newport monochromator (Newport Instruments). For water evaporation studies, bilayer PTFs and the control BNC foam with ~1.5 cm thickness and ~3 mm diameter were used. Bilayer PTFs were allowed to float on normal tap water in a beaker. The size of the beaker was selected to fit the fabricated PTF inside the beaker to ensure that no bare water surface was exposed to radiation. The approximate power density at the evaporating surface was kept as 1054 W m^{-2}. The mass loss corresponding to the evaporated water was calculated using an electronic weighing balance (Mettler Toledo, India). The temperature profiles before and after illumination were captured on an IR thermal imaging camera (FLIR E4, 250 W). The real-time analysis of the sample was performed outdoor under direct sunlight on a noncloudy sunny day (ambient temperature, 29 °C; humidity, 62%). The solar power intensity was continuously monitored every 30 min on a power meter, and the average value was considered for calculations. The evaporated water was collected under real-time conditions.

■ ASSOCIATED CONTENT

Supporting Information

The Supporting Information is available free of charge at https://pubs.acs.org/doi/10.1021/acsabm.1c00143.

SEM and XRD characterizations of BT powder; TEM and ATR-FTIR characterizations of BNC; demonstration of the floatability of PTFs; SEM images of PTFs with varying compositions; thermal profiles of fabricated PTFs with varying compositions; and BET and BJH analyses of PTF_b (PDF)

■ AUTHOR INFORMATION

Corresponding Authors

Syed Gulam Dastager − *Academy of Scientific and Innovative Research (AcSIR), Ghaziabad, Uttar Pradesh 201 002, India; CSIR-National Chemical Laboratory (NCL), Pune, Maharashtra 411008, India;* orcid.org/0000-0002-8316-1242; Email: sg.dastager@ncl.res.in

Saju Pillai − *Functional Materials, Materials Science and Technology Division, CSIR-National Institute for Interdisciplinary Science and Technology (NIIST), Thiruvananthapuram, Kerala 695 019, India; Academy of Scientific and Innovative Research (AcSIR), Ghaziabad, Uttar Pradesh 201 002, India;* orcid.org/0000-0001-9855-6899; Email: pillai_saju@niist.res.in

Authors

Kallayi Nabeela − *Functional Materials, Materials Science and Technology Division, CSIR-National Institute for Interdisciplinary Science and Technology (NIIST), Thiruvananthapuram, Kerala 695 019, India; Academy of Scientific and Innovative Research (AcSIR), Ghaziabad, Uttar Pradesh 201 002, India*

Meghana Namdeo Thorat − *Academy of Scientific and Innovative Research (AcSIR), Ghaziabad, Uttar Pradesh 201 002, India; CSIR-National Chemical Laboratory (NCL), Pune, Maharashtra 411008, India*

Sumina Nambooorimadathil Backer − *Functional Materials, Materials Science and Technology Division, CSIR-National Institute for Interdisciplinary Science and Technology (NIIST), Thiruvananthapuram, Kerala 695 019, India; Academy of Scientific and Innovative Research (AcSIR), Ghaziabad, Uttar Pradesh 201 002, India*

Animesh M. Ramachandran − *Functional Materials, Materials Science and Technology Division, CSIR-National Institute for Interdisciplinary Science and Technology (NIIST), Thiruvananthapuram, Kerala 695 019, India*

Reny Thankam Thomas − *Functional Materials, Materials Science and Technology Division, CSIR-National Institute for Interdisciplinary Science and Technology (NIIST), Thiruvananthapuram, Kerala 695 019, India*

Gopika Preethikumar − *Functional Materials, Materials Science and Technology Division, CSIR-National Institute for Interdisciplinary Science and Technology (NIIST), Thiruvananthapuram, Kerala 695 019, India*

A. Peer Mohamed − *Functional Materials, Materials Science and Technology Division, CSIR-National Institute for Interdisciplinary Science and Technology (NIIST), Thiruvananthapuram, Kerala 695 019, India*

Adersh Asok − *Functional Materials, Materials Science and Technology Division, CSIR-National Institute for Interdisciplinary Science and Technology (NIIST), Thiruvananthapuram, Kerala 695 019, India; Academy of Scientific and Innovative Research (AcSIR), Ghaziabad, Uttar Pradesh 201 002, India;* orcid.org/0000-0001-8718-9974

Complete contact information is available at: https://pubs.acs.org/10.1021/acsabm.1c00143

Author Contributions

‖K.N. and M.N.T. contributed equally to this work.

Author Contributions

The manuscript was written through contributions of all authors. All authors have given approval to the final version of the manuscript.

Notes

The authors declare no competing financial interest.

■ ACKNOWLEDGMENTS

K.N., S.N.B., and M.N.T. are thankful for financial support from the UGC grant and R.T.T. from a KSCSTEC-National postdoctoral fellowship (KSCSTEC/309/2018). This research was supported by a DST project [DST/TMD/MES/2K17/17(G)/1] and DBT (No. BT/PR11160/AAQ/3/674/2014).

REFERENCES

(1) Hu, X.; Zhu, J. Tailoring aerogels and related 3d macroporous monoliths for interfacial solar vapor generation. *Adv. Funct. Mater.* **2020**, *30*, No. 1907234.

(2) Zhang, Y.; Xiong, T.; Nandakumar, D. K.; Tan, S. C. Structure Architecting for Salt-Rejecting Solar Interfacial Desalination to Achieve High-Performance Evaporation With In Situ Energy Generation. *Adv. Sci.* **2020**, *7*, No. 1903478.

(3) Kashyap, V.; Ghasemi, H. Solar heat localization: concept and emerging applications. *J. Mater. Chem. A* **2020**, *8*, 7035−7065.

(4) Shi, L.; Wang, Y.; Zhang, L.; Wang, P. Rational design of a bi-layered reduced graphene oxide film on polystyrene foam for solar-driven interfacial water evaporation. *J. Mater. Chem. A* **2017**, *5*, 16212−16219.

(5) Tao, P.; Ni, G.; Song, C.; Shang, W.; Wu, J.; Zhu, J.; Chen, G.; Deng, T. Solar-driven interfacial evaporation. *Nat. Energy* **2018**, *3*, 1031−1041.

(6) Chang, C.; Yang, C.; Liu, Y.; Tao, P.; Song, C.; Shang, W.; Wu, J.; Deng, T. Efficient solar-thermal energy harvest driven by interfacial plasmonic heating-assisted evaporation. *ACS Appl. Mater. Interfaces* **2016**, *8*, 23412−23418.

(7) Wang, Y.; Zhang, L.; Wang, P. Self-floating carbon nanotube membrane on macroporous silica substrate for highly efficient solar-driven interfacial water evaporation. *ACS Sustainable Chem. Eng.* **2016**, *4*, 1223−1230.

(8) Zhu, L.; Gao, M.; Peh, C. K. N.; Ho, G. W. Recent progress in solar-driven interfacial water evaporation: advanced designs and applications. *Nano Energy* **2019**, *57*, 507−518.

(9) Zhu, L.; Gao, M.; Peh, C. K. N.; Wang, X.; Ho, G. W. Self-Contained Monolithic Carbon Sponges for Solar-Driven Interfacial Water Evaporation Distillation and Electricity Generation. *Adv. Energy Mater.* **2018**, *8*, No. 1702149.

(10) Tao, F.; Zhang, Y.; Yin, K.; Cao, S.; Chang, X.; Lei, Y.; Wang, D.; Fan, R.; Dong, L.; Yin, Y. A plasmonic interfacial evaporator for high-efficiency solar vapor generation. *Sustainable Energy Fuels* **2018**, *2*, 2762−2769.

(11) Shang, M.; Li, N.; Zhang, S.; Zhao, T.; Zhang, C.; Liu, C.; Li, H.; Wang, Z. Full-Spectrum Solar-to-Heat Conversion Membrane with Interfacial Plasmonic Heating Ability for High-Efficiency Desalination of Seawater. *ACS Appl. Energy Mater.* **2018**, *1*, 56−61.

(12) Yang, Y.; Zhao, R.; Zhang, T.; Zhao, K.; Xiao, P.; Ma, Y.; Ajayan, P. M.; Shi, G.; Chen, Y. Graphene-based standalone solar energy converter for water desalination and purification. *ACS Nano* **2018**, *12*, 829−835.

(13) Jiang, Q.; Tian, L.; Liu, K. K.; Tadepalli, S.; Raliya, R.; Biswas, P.; Naik, R. R.; Singamaneni, S. Bilayered biofoam for highly efficient solar steam generation. *Adv. Mater.* **2016**, *28*, 9400−9407.

(14) Zhu, B.; Kou, H.; Liu, Z.; Wang, Z.; Macharia, D. K.; Zhu, M.; Wu, B.; Liu, X.; Chen, Z. Flexible and Washable CNT-Embedded PAN Nonwoven Fabrics for Solar-Enabled Evaporation and Desalination of Seawater. *ACS Appl. Mater. Interfaces* **2019**, *11*, 35005−35014.

(15) Bae, K.; Kang, G.; Cho, S. K.; Park, W.; Kim, K.; Padilla, W. J. Flexible thin-film black gold membranes with ultrabroadband plasmonic nanofocusing for efficient solar vapour generation. *Nat. Commun.* **2015**, *6*, No. 10103.

(16) Wang, Z.; Liu, Y.; Tao, P.; Shen, Q.; Yi, N.; Zhang, F.; Liu, Q.; Song, C.; Zhang, D.; Shang, W. Bio-Inspired Evaporation Through Plasmonic Film of Nanoparticles at the Air−Water Interface. *Small* **2014**, *10*, 3234−3239.

(17) Li, R.; Zhang, L.; Shi, L.; Wang, P. MXene Ti_3C_2: an effective 2D light-to-heat conversion material. *ACS Nano* **2017**, *11*, 3752−3759.

(18) Gao, M.; Zhu, L.; Peh, C. K.; Ho, G. W. Solar absorber material and system designs for photothermal water vaporization towards clean water and energy production. *Energy Environ. Sci.* **2019**, *12*, 841−864.

(19) Chen, X.; Liu, L.; Peter, Y. Y.; Mao, S. S. Increasing solar absorption for photocatalysis with black hydrogenated titanium dioxide nanocrystals. *Science* **2011**, *331*, 746−750.

(20) Liu, Y.; Tian, L.; Tan, X.; Li, X.; Chen, X. Synthesis, properties, and applications of black titanium dioxide nanomaterials. *Sci. Bull.* **2017**, *62*, 431−441.

(21) Chen, X.; Liu, L.; Liu, Z.; Marcus, M. A.; Wang, W.-C.; Oyler, N. A.; Grass, M. E.; Mao, B.; Glans, P.-A.; Peter, Y. Y. Properties of disorder-engineered black titanium dioxide nanoparticles through hydrogenation. *Sci. Rep.* **2013**, *3*, No. 1510.

(22) Zhu, G.; Xu, J.; Zhao, W.; Huang, F. Constructing black titania with unique nanocage structure for solar desalination. *ACS Appl. Mater. Interfaces* **2016**, *8*, 31716−31721.

(23) Nambooorimadathil Backer, S.; Ramachandran, A. M.; Venugopal, A. A.; Mohamed, A.; Asok, A.; Pillai, S. Clean Water from Air Utilizing Black TiO2-based Photothermal Nanocomposite Sheets. *ACS Appl. Nano Mater.* **2020**, *3*, 6827−6835.

(24) Chen, C.; Kuang, Y.; Hu, L. Challenges and opportunities for solar evaporation. *Joule* **2019**, *3*, 683−718.

(25) Yang, Y.; Yang, X.; Fu, L.; Zou, M.; Cao, A.; Du, Y.; Yuan, Q.; Yan, C.-H. Two-dimensional flexible bilayer Janus membrane for advanced photothermal water desalination. *ACS Energy Lett.* **2018**, *3*, 1165−1171.

(26) Ito, Y.; Tanabe, Y.; Han, J.; Fujita, T.; Tanigaki, K.; Chen, M. Multifunctional porous graphene for high-efficiency steam generation by heat localization. *Adv. Mater.* **2015**, *27*, 4302−4307.

(27) Zhao, F.; Zhou, X.; Shi, Y.; Qian, X.; Alexander, M.; Zhao, X.; Mendez, S.; Yang, R.; Qu, L.; Yu, G. Highly efficient solar vapour generation via hierarchically nanostructured gels. *Nat. Nanotechnol.* **2018**, *13*, 489−495.

(28) Zhou, X.; Zhao, F.; Guo, Y.; Rosenberger, B.; Yu, G. Architecting highly hydratable polymer networks to tune the water state for solar water purification. *Sci. Adv.* **2019**, *5*, No. eaaw5484.

(29) Zhou, X.; Guo, Y.; Zhao, F.; Yu, G. Hydrogels as an emerging material platform for solar water purification. *Acc. Chem. Res.* **2019**, *52*, 3244−3253.

(30) Li, T.; Fang, Q.; Lin, H.; Liu, F. Enhancing solar steam generation through manipulating the heterostructure of PVDF membranes with reduced reflection and conduction. *J. Mater. Chem. A* **2019**, *7*, 17505−17515.

(31) Jiang, M.; Shen, Q.; Zhang, J.; An, S.; Ma, S.; Tao, P.; Song, C.; Fu, B.; Wang, J.; Deng, T. Bioinspired Temperature Regulation in Interfacial Evaporation. *Adv. Funct. Mater.* **2020**, *30*, No. 1910481.

(32) Li, B.; Han, C.; He, Y.; Yang, C.; Du, H.; Yang, Q.; Kang, F. Facile synthesis of $Li_4Ti_5O_{12}$/C composite with super rate performance. *Energy Environ. Sci.* **2012**, *5*, 9595−9602.

(33) Ma, S.; Chiu, C. P.; Zhu, Y.; Tang, C. Y.; Long, H.; Qarony, W.; Zhao, X.; Zhang, X.; Lo, W. H.; Tsang, Y. H. Recycled waste black polyurethane sponges for solar vapor generation and distillation. *Appl. Energy* **2017**, *206*, 63−69.

(34) Huang, H.; Zhao, L.; Yu, Q.; Lin, P.; Xu, J.; Yin, X.; Chen, S.; Wang, H.; Wang, L. Flexible and Highly Efficient Bilayer Photothermal Paper for Water Desalination and Purification: Self-Floating, Rapid Water Transport, and Localized Heat. *ACS Appl. Mater. Interfaces* **2020**, *12*, 11204−11213.

(35) Liu, Y.; Yu, S.; Feng, R.; Bernard, A.; Liu, Y.; Zhang, Y.; Duan, H.; Shang, W.; Tao, P.; Song, C. A bioinspired, reusable, paper-based system for high-performance large-scale evaporation. *Adv. Mater.* **2015**, *27*, 2768−2774.

(36) Liu, K.-K.; Jiang, Q.; Tadepalli, S.; Raliya, R.; Biswas, P.; Naik, R. R.; Singamaneni, S. Wood−Graphene Oxide Composite for Highly Efficient Solar Steam Generation and Desalination. *ACS Appl. Mater. Interfaces* **2017**, *9*, 7675−7681.

(37) Xue, G.; Liu, K.; Chen, Q.; Yang, P.; Li, J.; Ding, T.; Duan, J.; Qi, B.; Zhou, J. Robust and Low-Cost Flame-Treated Wood for High-Performance Solar Steam Generation. *ACS Appl. Mater. Interfaces* **2017**, *9*, 15052−15057.

(38) Ghim, D.; Jiang, Q.; Cao, S.; Singamaneni, S.; Jun, Y.-S. Mechanically interlocked 1T/2H phases of MoS2 nanosheets for solar thermal water purification. *Nano Energy* **2018**, *53*, 949−957.

(39) Jiang, Q.; Derami, H. G.; Ghim, D.; Cao, S.; Jun, Y.-S.; Singamaneni, S. Polydopamine-filled bacterial nanocellulose as a

https://doi.org/10.1021/acsabm.1c00143
ACS Appl. Bio Mater. XXXX, XXX, XXX−XXX

biodegradable interfacial photothermal evaporator for highly efficient solar steam generation. *J. Mater. Chem. A* **2017**, *5*, 18397−18402.
(40) Jiang, F.; Liu, H.; Li, Y.; Kuang, Y.; Xu, X.; Chen, C.; Huang, H.; Jia, C.; Zhao, X.; Hitz, E. Lightweight, mesoporous, and highly absorptive all-nanofiber aerogel for efficient solar steam generation. *ACS Appl. Mater. Interfaces* **2018**, *10*, 1104−1112.
(41) Li, Y.; Zhu, H.; Shen, F.; Wan, J.; Lacey, S.; Fang, Z.; Dai, H.; Hu, L. Nanocellulose as green dispersant for two-dimensional energy materials. *Nano Energy* **2015**, *13*, 346−354.
(42) Cao, S.; Rathi, P.; Wu, X.; Ghim, D.; Jun, Y. S.; Singamaneni, S. Cellulose Nanomaterials in Interfacial Evaporators for Desalination: A "Natural" Choice. *Adv. Mater.* **2020**, No. 2000922.
(43) Santmarti, A.; Lee, K.-Y. Crystallinity and Thermal Stability of Nanocellulose. *Nanocellulose Sustainability* **2018**, 67−86.
(44) Vitta, S.; Thiruvengadam, V. Multifunctional bacterial cellulose and nanoparticle-embedded composites. *Curr. Sci.* **2012**, *102*, 1398−1405.
(45) Yang, J.; Pang, Y.; Huang, W.; Shaw, S. K.; Schiffbauer, J.; Pillers, M. A.; Mu, X.; Luo, S.; Zhang, T.; Huang, Y. Functionalized graphene enables highly efficient solar thermal steam generation. *ACS Nano* **2017**, *11*, 5510−5518.
(46) Hu, X.; Xu, W.; Zhou, L.; Tan, Y.; Wang, Y.; Zhu, S.; Zhu, J. Tailoring graphene oxide-based aerogels for efficient solar steam generation under one sun. *Adv. Mater.* **2017**, *29*, No. 1604031.
(47) Zhang, D.; Cai, Y.; Liang, Q.; Wu, Z.; Sheng, N.; Zhang, M.; Wang, B.; Chen, S. Scalable, Flexible, Durable, and Salt-Tolerant CuS/Bacterial Cellulose Gel Membranes for Efficient Interfacial Solar Evaporation. *ACS Sustainable Chem. Eng.* **2020**, *8*, 9017−9026.
(48) Liu, S.; Huang, C. A stable and flexible carbon black/polyethyleneimine-bacterial cellulose photothermal membrane for high-efficiency solar vapor generation. *Int. J. Energy Res.* **2020**, *44*, 8904−8918.
(49) Sumina, N.; Kumar, S. N.; Achu, R.; Kumar, B. D.; Ray, A. K.; Warrier, K.; Pillai, S. Low Temperature Synthesis of High Energy Facets Exposed Sheet−like Anatase TiO2 Mesocrystals Show Reduced e−/h+ Pair Recombination Rates and Enhanced Photoactivity. *ChemistrySelect* **2016**, *1*, 6221−6229.
(50) Thorat, M. N.; Dastager, S. G. High yield production of cellulose by a *Komagataeibacter rhaeticus* PG2 strain isolated from pomegranate as a new host. *RSC Adv.* **2018**, *8*, 29797−29805.
(51) Rongpipi, S.; Ye, D.; Gomez, E. D.; Gomez, E. W. Progress and Opportunities in the Characterization of Cellulose−An Important Regulator of Cell Wall Growth and Mechanics. *Front. Plant Sci.* **2019**, *9*, No. 1894.
(52) Vazquez, A.; Foresti, M. L.; Cerrutti, P.; Galvagno, M. Bacterial cellulose from simple and low cost production media by Gluconacetobacter xylinus. *J. Polym. Environ.* **2013**, *21*, 545−554.
(53) Lee, C. M.; Mittal, A.; Barnette, A. L.; Kafle, K.; Park, Y. B.; Shin, H.; Johnson, D. K.; Park, S.; Kim, S. H. Cellulose polymorphism study with sum-frequency-generation (SFG) vibration spectroscopy: identification of exocyclic CH 2 OH conformation and chain orientation. *Cellulose* **2013**, *20*, 991−1000.
(54) Shi, Y.; Li, R.; Jin, Y.; Zhuo, S.; Shi, L.; Chang, J.; Hong, S.; Ng, K.-C.; Wang, P. A 3D photothermal structure toward improved energy efficiency in solar steam generation. *Joule* **2018**, *2*, 1171−1186.
(55) Nabeela, K.; Thomas, R. T.; Nair, J. B.; Maiti, K. K.; Warrier, K. G. K.; Pillai, S. TEMPO-Oxidized Nanocellulose Fiber-Directed Stable Aqueous Suspension of Plasmonic Flower-like Silver Nanoconstructs for Ultra-Trace Detection of Analytes. *ACS Appl. Mater. Interfaces* **2016**, *8*, 29242−29251.
(56) Nabeela, K.; Thomas, R. T.; Mohamed, A.; Pillai, S. Nanocellulose-silver ensembles for ultrasensitive SERS: An investigation on the role of nanocellulose fibers in the generation of high-density hotspots. *Appl. Mater. Today* **2020**, *20*, No. 100672.
(57) Ghasemi, H.; Ni, G.; Marconnet, A. M.; Loomis, J.; Yerci, S.; Miljkovic, N.; Chen, G. Solar steam generation by heat localization. *Nat. Commun.* **2014**, *5*, No. 4449.

https://doi.org/10.1021/acsabm.1c00143
ACS Appl. Bio Mater. XXXX, XXX, XXX−XXX